Office de la Propriété Intellectuelle du Canada
Un organisme d'Industrie Canada

Canadian Intellectual Property Office
An agency of Industry Canada

CA 2846963 A1 2015/09/14

(21) 2 846 963

(12) DEMANDE DE BREVET CANADIEN
CANADIAN PATENT APPLICATION

(13) A1

(22) Date de dépôt/Filing Date: 2014/03/14

(41) Mise à la disp. pub./Open to Public Insp.: 2015/09/14

(51) Cl.Int./Int.Cl. *B01J 19/08* (2006.01), *B01J 19/02* (2006.01), *B81B 1/00* (2006.01), *B82Y 30/00* (2011.01), *C12M 1/34* (2006.01), *C12M 1/38* (2006.01), *C12P 19/34* (2006.01), *C12Q 1/68* (2006.01)

(71) Demandeur/Applicant:
UTI LIMITED PARTNERSHIP, CA

(72) Inventeurs/Inventors:
KALER, KARAN, CA;
PRAKASH, RAVI, CA

(74) Agent: GOWLING LAFLEUR HENDERSON LLP

(54) Titre : DISPOSITIF MICROFLUIDIQUE A GOUTELETTES ET SES METHODES DE PRODUCTION ET D'UTILISATION
(54) Title: DROPLET-BASED MICROFLUIDIC DEVICE AND METHODS FOR PRODUCING AND USING THE SAME

(57) Abrégé/Abstract:
The present invention provides a droplet-based microfluidic device comprising a passivating top surface and methods for producing and using the same. In particular, the passivating surface comprises of a nano-textured superhydrophobic material.

ABSTRACT

The present invention provides a droplet-based microfluidic device comprising a passivating top surface and methods for producing and using the same. In particular, the passivating surface comprises of a nano-textured superhydrophobic material.

DROPLET-BASED MICROFLUIDIC DEVICE AND METHODS FOR PRODUCING AND USING THE SAME

FIELD OF THE INVENTION

[0001] The present invention relates to a droplet-based microfluidic device comprising superhydrophobic coating and methods for producing and using the same. In particular, the microfluidic devices of the invention include a single substrate with structured micro-electrodes, dielectric passivation and a top nano-textured superhydrophobic coating.

BACKGROUND OF THE INVENTION

[0002] Miniaturized bio-diagnostic devices have the potential to allow for rapid pathogen screening in clinical patient samples, as a low cost and portable alternative to conventional bench-top equipment. Miniaturization of key bio-diagnostic techniques, such as: nucleic acid detection and quantification, nucleic acid amplification test (NAAT), polymerase chain reaction (PCR), DNA fingerprinting, enzyme linked immunosorbent assay (ELISA), results in substantial reduction of reaction volumes (expensive samples/reagents) and shorter reaction times.

[0003] Droplet microfluidics (DMF) is one of several miniaturized bio-sample handling techniques available for manipulating clinical samples and reagents in microliter (10^{-6}L) to picoliter (10^{-12} L) volume. Electro-actuation of sample and reagent in the form of droplets using dielectrophoresis (DEP) and/or Electrowetting (EW) are achieved by means of patterned, insulated metal electrodes on one or more substrates.

[0004] Unfortunately, due to the commonly used surface materials of conventional DMF devices, sample handling using conventional DMF devices result in some of the sample being left behind on the surface of DMF during manipulation of liquid droplets as a result of surface adsorption. This results in requiring addition of pluronics®, which are bio-compatible surfactants, or a special top coating that can alleviate the sample adsorption issues.

[0005] Accordingly, there is a need for DMF devices that are produced with a tailored top superhydrophobic surface. There is also a need for a method for producing such DMF devices.

SUMMARY OF THE INVENTION

[0006] Some aspects of the invention provide a droplet-based microfluidic device comprising a substrate having a surface; a plurality of micro-electrodes patterned on said surface, wherein said plurality of micro-electrodes are configured to confine, electrically actuate and transport liquid droplets; and a passivating surface coated onto said plurality of micro-electrodes, wherein said passivating surface comprises a superhydrophobic material. In some embodiments, said superhydrophobic material comprises fluoropolymer. Exemplary fluoropolymers that are useful for DMF devices of the invention include, but are not limited to, fluorocarbon (e.g., TEFLON®), fluorosilane and CYTOP®. Typically, DMF devices of the invention include a nano-textured dielectric layer (Si_3N_4, SiO_2 etc.). Often the fluoropolymer is coated onto the substrate (i.e., dielectric, often nano-textured dielectric layer) by plasma deposition, spin-coating or, a combination thereof.

[0007] The substrate typically comprises a dielectric material. Suitable dielectric materials for the substrate include, but are not limited to, silicon oxide and silicon nitride. It should be appreciated that the substrate can be made of one or more of the dielectric materials. Typically, the substrate is nano-textured. As used herein, the term "nano-textured" means the surface of the substrate is not smooth, but a rough or, raised texture, which is in nanometer scale. Typically, the height of raised texture is about 300 nm or less, often about 250 nm or less, and more often about 200 nm or less. In general, the texture is a regular repeating shape. However, it should be appreciated that nano-texture can be irregular and/or non-repeating shape.

[0008] In some embodiments, said passivated surface is nano-textured. The nano-textured superhydrophobic material is adapted to prevent adsorption, sample loss and/or collapse of liquid droplets.

[0009] Yet in other embodiments, the droplet-based microfluidic device of the invention further comprises at least one reaction chamber area that is configured to allow a chemical reaction to occur within said reaction chamber area. The reaction chamber is connected to at least one set of the said plurality of micro-electrodes. This allows transfer of droplets to the reaction chamber area by actuation of micro-electrodes.

[0010] Still in other embodiments, the droplet-based microfluidic device of the invention further comprises one or more, e.g., at least two, typically at least three, and often a plurality of, heating elements that are operatively connected to the said reaction chamber area. The heating elements are configured to provide the necessary reaction temperatures within said reaction chamber area during its use, e.g., such as bio-assay, polymerase chain reaction (PCR), chemical synthesis, etc.

[0011] In other embodiments, the droplet-based microfluidic device of the invention further comprises one or more, e.g., at least two, typically at least three, and often a plurality of, temperature detector elements configured to detect the temperature zones within the said reaction chamber area. In some instances, the temperature detector element can be operatively connected to the heating element such that the heating element can be actuated based on the temperature detected by the temperature detector element. Generally, each reaction chamber area has its own set of heating element and temperature detector element.

[0012] Yet still in other embodiments, the droplet-based microfluidic device of the present invention further comprises at least one reagent reservoir area operatively connected to said reaction chamber area. In this manner, the reagent or the sample can be placed in the reagent reservoir area and can be transferred to a reaction chamber area by actuating the plurality of micro-electrodes.

[0013] The droplet-based microfluidic ("DMF") device of the invention can be used in a variety of applications such as for conducting a polymerase chain reaction (including real-time polymerase chain reaction and/or quantitative polymerase chain reaction and other nucleic acid amplification reactions), a clinical diagnostic assay.

[0014] Still yet in other embodiments, the contact angle of a water droplet on said superhydrophobic material is at least 150°, typically at least 155°.

[0015] Yet in other embodiments, the DMF devices of the invention can include a plurality of reaction chamber areas that are configured to allow simultaneous chemical reactions to occur within each of said reaction chamber area. In some instances, DMF devices of the invention also comprises a plurality of heating elements, wherein each of said heating element is operatively connected to each of said reaction chamber area. Typically, each of said heating

element is independently configured to provide the necessary temperature zone within each of said reaction chamber area upon actuation. It should be appreciated that the temperature within each temperature zone is independent of the other temperature zones. This configuration allows different temperature zones within a single DMF device. Yet in other instances, DMF device of the invention comprises a plurality of temperature detector elements. Typically, each of said temperature detector element is individually configured to detect the temperature zone within each of said plurality of reaction chamber areas.

[0016] In other embodiments, DMF device of the invention is configured for quantitative polymerase chain reaction. Yet in other embodiments, DMF device of the invention is configured for amplifying nucleic acids. Still in other embodiments, DMF device of the invention is configured for conducting clinical diagnostic assay. Other embodiments include DMF device of the invention that is configured for conducting real-time, quantitative polymerase chain reaction. Regardless of the use (e.g., clinical assay, PCR, chemical reaction, RT-PCR, etc.) DMF devices of the invention can be configured for a plurality of simultaneous (e.g., parallel) or step-wise (e.g., series) uses such as real-time, quantitative polymerase chain reactions in parallel by simply having a sufficient or necessary number of reaction chamber areas and corresponding heating elements, and/or temperature detector elements. See, for example, Figure 23.

BRIEF DESCRIPTION OF THE DRAWINGS

[0017] Figure 1: Model geometry of micro heater design and COMSOL simulation results for optimized micro-heater electrode architecture, showing and steady state thermal profile for the 95 °C heating zone.

[0018] Figure 2: Standard temperature calibration curve for the designed RTD sensor extracted before the chip based qRT-PCR assay.

[0019] Figure 3: (a) Two surface EW electrode array for droplet manipulation [13]; (b) Droplet transport (1 μL, de-ionized water) using a single surface, herring-bone shaped D-DEP electrode structure (pitch: 100 μm; gap: 10 μm).

[0020] Figure 4: Schematic flow chart of the micro-fabrication process, implemented to realize the designed qRT-PCR micro-devices. (PECVD = Plasma Enhanced Chemical Vapor Deposition, RIE = reactive ion etching)

[0021] Figure 5: Schematic of the experimental set-up and snapshot of the microfluidic chip-PCB assembly.

[0022] Figure 6: Schematic diagram and photomicrographs showing the electrode architecture of the two different RT-PCR micro-devices.

[0023] Figure 7: Snapshots extracted from a PCR droplet actuation video, of the qRT-PCR reaction using micro-electrode 1. PCR droplet actuated using 90 V_{pp} at 60 Hz AC signal.

[0024] Figure 8: Snapshots of qRT-PCR droplet actuation over micro-electrode 2. Applied AC signal for droplet actuation: 120 V_{pp} at 90 Hz for EW and 90 V_{pp} @ 60 Hz for D-DEP electrodes.

[0025] Figure 9: qRT-PCR experimental data for different influenza C RNA samples actuated using micro-electrode 1.

[0026] Figure 10: Results of the chip based qRT-PCR amplification and detection of influenza A virus using micro-electrode 2.

[0027] Figure 11: Standard quantification curves for chip based qRT-PCR amplification of influenza A and C RNA samples.

[0028] Figure 12: Outcomes of the chip based qRT-PCR assays using different PCR droplet volumes.

[0029] Figure 13: (a) Schematic image of close packed polystyrene (PS) microbeads (top view); (b) PS shrinkage during colloidal lithography process; (c) cross-sectional view of the nano-patterned LDEP device.

[0030] Figure 14: SEM images illustrating the various stages of fabrication during the nano-patterning.

[0031] Figure 15: CA of a 5 mL droplet (a) for composite FC coated surface, (b) for ϕ_s = 0.51, h_p = 100 nm and (c) for ϕ_s = 0.15, h_p = 180 nm.

[0032] Figure 16: Experimental results and theoretical data, extracted from the developed lumped model for estimation of minimum LDEP actuation voltage (V_{min}) and using a model equation for the required threshold actuation voltage during LDEP actuation in air, of different Tw-DI sample concentrations (see Table 2-2) over both (a) SH and (c) hydrophobic surfaces.

[0033] Figure 17: Comparison of the experimental and the theoretical data, extracted using the solution to the developed lumped model, for the transient behavior of LDEP actuations in air; (a, b) actuated jet length (z) vs. time (t) and z vs. $t^{1/2}$ plots for actuation over hydrophobic surface; (c, d) z vs. t and z vs. $t^{1/2}$ plots for actuation over SH surface. The z vs. $t^{1/2}$ plots shown in b and d correspond to the initial liquid actuation period of ~40 ms.

[0034] Figure 18: Equivalent lumped capacitance model for analyzing the DEP force term.

[0035] Figure 19: (a–c) Micrographs showing LDEP actuation in a 5 cSt silicone oil bath, on a hydrophobic surface and, (d–f) on the SH surface with identical electrode geometry.

[0036] Figure 20: Effect of TAQ enzyme adsorption on composite coated hydrophobic surface and SH surface, analyzed in terms of: (a) loss of enzyme concentration due to adsorption from the parent droplet and, (b) reduction in droplet CAs, measured between repeated LDEP actuations. Droplet CA values in (b) are averaged over 6–8 droplets with a standard deviation of 5◦, reported as error bars in the plots

[0037] Figure 21: Images comparing the performance of a hydrophobic LDEP device during first (a, b) and second (c–f) LDEP actuation.

[0038] Figure 22: Micrographs showing LDEP actuation of 0.35 mg/mL TAQ DNA polymerase droplet over a SH LDEP device.

[0039] Figure 23 shows an exemplary DMF device of the invention configured for carrying out multiplex qRT-PCR.

DETAILED DESCRIPTION OF THE INVENTION

[0040] While the close channel microfluidic chips clearly have established their usefulness of chip based sample manipulation, e.g., PCR amplification of nucleic acids, clinical diagnostic assays and micro-scale chemical reactions, using these close channel microfluidics

suffer from various problems, such as the requirement of valves and micro-tubes for sample loading and fluidic control, sample or reagent adsorption in the exposed microfluidic channels etc. Droplet based PCR has recently emerged as an alternative method for on-chip PCR reactions. In this method, PCR droplets are thermal cycled by either keeping the droplet stationary in a variable temperature control zone (static droplet PCR) or by moving the droplet continuously between two or more different temperature control zones (transport-based droplet PCR). The transport-based droplet PCR technique is in many ways superior to the static method due to its shorter temperature ramp times, resulting in fast and more efficient chip based PCR reactions. However, during a transport-based droplet PCR, some of the samples and/or reagents can be lost due to adsorption or the droplet can collapse during transport.

[0041] Some aspects of the invention provide transport-based droplet microfluidic (DMF) devices that eliminate or significantly reduce the amount of sample and/or reagent adsorption. In particular, some aspects of the invention provide electro-actuation based droplet microfluidic (DMF) devices and methods for using the same. DMF devices of the invention include a substrate having a surface; a plurality of micro-electrodes patterned on said surface; and a passivating surface coated onto said plurality of micro-electrodes. The plurality of micro-electrodes are configured to confine, electrically actuate and transport liquid droplets. The passivating surface includes a superhydrophobic material. The superhydrophobic material allows an aqueous solution of liquid droplet samples or reagents to be manipulated within the DMF devices of the invention without any significant loss of samples/reagents due to surface adsorption. Typically, the amount of sample loss due to surface adsorption is about 6% or less, often about 5.5% or less, and most often about 4% or less. More significantly, there is no droplet collapse (e.g., of aqueous solution) on the surface of DMF devices of the invention.

[0042] DMF devices of the invention can be configured and integrated with suitably tailored micro-heaters and temperature sensors, to achieve chip based real-time, quantitative PCR (qRT-PCR) as well as other suitable chemical reactions, clinical diagnostic assays, etc. For the sake of clarity and brevity, the present invention will now be described in reference to conducting PCR and clinical diagnostic assays. However, it should be appreciated that the scope of the invention is not limited to using DMF devices of the invention for PCR and clinical diagnostic assays.

[0043] In one particular embodiment, The DMF device of the invention was used in qRT-PCR. Yet in another embodiment, the DMF device of the invention was utilized to detect and quantify the presence of influenza A and C virus nucleic acids, e.g., by using in-vitro synthesized viral RNA segments. In particular, the experimental analysis of the DMF device confirms its capabilities in qRT-PCR based detection and quantification of pathogen samples, with high accuracy levels. In some embodiments, DMF devices of the invention result in PCR efficiency of at least 94 %, typically at least 95 %, and often at least 96%. The limit of detection (LOD) for the chip based qRT-PCR technique using DMF device of the invention is about 10 copies or less, typically about 5 copies or less, and often 3 copies or less of template RNA per PCR reaction.

[0044] Influenza viruses, which belong to the family *Orthomyxoviridae*, are pathogens of humans and animals [1]. Influenza viruses from three different genera are currently circulating in the human population: influenza A, influenza B and influenza C viruses. Of these, influenza A viruses have the greatest impact on the population, in terms of severity of disease and because of their greater capacity to generate new strains through a high rate of mutagenesis causing genetic drift. Influenza A viruses originated from wild aquatic birds whose population contains a very large reservoir of influenza A viruses from which new emerging strains can enter the human population, directly or through another species such as swine. These emerging influenza A viruses can on occasion trigger pandemics, the worst of which, to date, was the 1918 "Spanish Flu" pandemic which was also the worst natural disaster of the 20th century [1]. Influenza C is a more benign pathogen than influenza A or B, in term of severity of disease and reported cases; however, it is under-diagnosed and underestimated because most clinical laboratories do not test for this agent. Recently, the importance of this agent was investigated [2].

[0045] Testing for influenza viruses is often required for patient care and is of the utmost public health importance. Molecular techniques, such as polymerase chain reaction (PCR) [3, 4], and immunoassays [5] have now become the methods of choice for pathogen screening. Real time, quantitative, reverse transcription polymerase chain reaction (qRT-PCR), which uses the well-known PCR technique for DNA amplification along with a specific molecular probe that allows for target detection in real time [6]. When this technique is brought to bear on RNA targets, such as the genome of influenza viruses, a preliminary step of "reverse transcription" is

required to transcribe the RNA segment into a complementary DNA (cDNA) segment. Nowadays, this is almost always done through a "one tube" technique, involving a reaction mixture containing both a reverse transcriptase enzyme and a thermostable DNA polymerase, with the two enzymatic reactions performed serially through temperature control [7].

[0046] For influenza A testing, some have adapted an assay designed and implemented by the Centers for Disease Control, as described in [8], and which uses the common methodology of hydrolysis probe for detection [6]. For influenza C, the real time RT-PCR method described by K. Pabbaraju et al., in *Influenza Other Resp Viruses*, doi: 10.1111/irv.12099 (2013), has been validated to work with either a hydrolysis probe or a beacon probe [6]. The beacon probe has the property that it can be used for both real time detection and post amplification detection, which was a useful stepping stone in some preliminary chip based post amplification viral screening experiments, not detailed in this report [9].

[0047] Miniaturization of nucleic acid amplification based pathogen detection methods promises to reduce the cost of these bio-assays by utilizing ultra-low volume of samples/reagents (μL to pL), and furthermore enable shorter turnaround time (sample-to-detection time) due to faster reaction kinetics at the miniaturized scale. Such PCR micro-devices can either be implemented using conventional close channel microfluidic [10, 11, 12] or droplet microfluidic technologies [13, 14, 15, 16, 17]. Chip based PCR amplification using close channel microfluidics was first to be explored [10, 12, 18, 19, 20]; however, such methods suffer from problems such as: the requirement of valves and micro-tubes for sample loading and fluidic control, bio-adsorption in the exposed microfluidic channels etc. The close channel microfluidic PCR chips clearly established the potential of chip based PCR technology. Droplet based PCR [21, 22] has recently emerged as a more popular alternative method for on-chip PCR reactions. In this method, PCR droplets are thermal cycled by either keeping the droplet stationary in a variable temperature control zone (static droplet PCR) [22, 23] or by moving the droplet continuously between two or more different temperature control zones (transport based droplet PCR) [21]. The transport based droplet PCR technique is in many ways superior to the static method due to its shorter temperature ramp times, resulting in fast and more efficient chip based PCR reactions.

[0048] Some aspects of the invention provide electro-actuation based DMF devices, where electric field effects are utilized for dispensing and subsequent handling of droplets comprising PCR samples and reagents. The DMF electro-actuation method provides precision dispensing, transport and mixing capability of ultrafine PCR reaction volumes over patterned surfaces. The two electro-actuation techniques: Electrostatic/Droplet dielectrophoresis (D-DEP) [16, 17] and Electrowetting (EW) [13, 14] have been used through tailored micro-electrode architectures to facilitate the required on-chip droplet manipulation. A different set of micro-electrode pattern was used to create resistive micro-heaters [23, 24] and resistance temperature detectors (RTDs) [24], required during the PCR thermal cycling. A nano-textured super hydrophobic (SH) surface [25] was engineered in order to prevent sample adsorption and droplet collapse, during the on-chip qRT-PCR detection. Performance of the integrated DMF device was analyzed in real-time chip based qRT-PCR detection of in-vitro synthesized influenza A and C virus RNAs during 30-35 PCR cycles. Experiments described herein demonstrate the utility of the electro-actuation based qRT-PCR micro-device for detecting and quantifying the presence of viral nucleic acids. In some embodiments, a detection threshold (limit of detection) of < 5 viral nucleic acid copies per PCR reaction was achieved.

[0049] In some embodiments, the DMF micro-device of the invention is comprised of, and integrates liquid sample handling and temperature control. The PCR samples/reagents were controlled using tailored microfluidic electrode structures that were energized by low frequency (30-90 Hz), AC voltage (50-120 V_{pp}), whereas the temperature control was achieved by means of resistive micro-heaters and resistive temperature detection (RTD) sensor electrode structures.

[0050] Temperature control is essential for an integrated PCR micro-device since performance of PCR reaction is greatly impacted by the temperature set-points and sample temperature ramp rates during thermal cycling [7, 10]. Poor temperature control can result in low PCR efficiency and non-specific probe-target DNA binding and amplification. Methods for chip-based temperature control can be classified as: contact or non-contact. In non-contact temperature control methods [26, 27], heating and temperature cycling is achieved by using schemes such as: selective infrared heating [26], laser induced heating [27] and thermocouple temperature sensing. Although effective, such methods often require specialized heating equipment (laser sources and other optical components) and additional temperature reference

chamber (for accurate temperature measurement), which results in complicated micro-device design and relatively lower degree of integration and miniaturization. Contact temperature control methods can utilize commercial thermo-cycler, Peltier thermoelectric element designs [28] to achieve nearly the same thermal conditions as in case of the conventional PCR set-up. More recently, as an alternative, commercial micro-heaters and thermocouples have been integrated with microfluidic platform to create PCR microsystems [28]. Though having excellent performances, this micro-device requires manual placement/integration of commercial heaters and thermocouples, to the back side of the microfluidic chip, resulting in reproducibility problems related to their manual placement. As an alternative, micro-heaters and resistance temperature detectors (RTDs) sensors can be micro-fabricated on the same substrate, along with the microfluidic electrodes, to create a more compact PCR micro-device [23, 24]. These integrated thermal elements improved the overall thermal transfer from the heating element to the PCR chamber and increased the accuracy as well as the reproducibility of the required temperature. Among the contact temperature control methods, the micro-fabricated resistive heaters/RTDs have smaller power requirement, faster thermal response and higher heating ramp rates. Accordingly, some DMF devices of the invention include one or more resistive heaters and RTDs.

[0051] In some embodiments, the micro-heater and RTDs were micro-fabricated using thin, patterned electrodes of Chromium. Chromium was selected due to its high resistivity (ρ: 12.9 μΩ–cm), temperature coefficient of resistance (α = 3000 ppm/°C) and its superior adhesion to the substrate of choice (Borofloat Glass). Contact pads and electrical connections were fabricated using Au/Cr layer to minimize their resistive contribution. Size and shape of the micro-heater electrode was optimized using COMSOL Multiphysics software's Heat transfer module (version 4.2). The micro-heater was designed to operate under a 'constant voltage' condition which relates the electrical power (P) for the resistive micro-heater as:

$$P = \frac{V^2}{R};\ \text{where } R = \frac{\rho L}{A} \qquad (1)$$

In Eqn. 1, 'L' and 'A' are respectively the total length and cross-sectional area of the micro-heater electrode. Dimensions of the designed micro-heater were optimized to reduce the voltage needed to generate the required thermal zones. The power/energy requirement of the micro-heater was modeled using the fundamental heat transfer expression:

$$dH = C_p(vD)dT \qquad (2)$$

where v is the PCR droplet volume, D is the sample density, C_p is the heat capacity of water (Cp ~ 4.2 J/g/°C) and dT being the required change in droplet temperature. For a 100 % efficient micro-heater, the power requirement can be estimated as: ($P = dH / dt$). To more accurately estimate the power requirement for each thermal zone, the micro-heater design was modeled in COMSOL (v. 4.2), for each thermal zone to maintain the optimum thermal zones during the PCR thermal cycling.

[0052] Figure 1 shows the results of the COMSOL simulation for the resistive micro-heater. Serpentine electrode geometry was utilized to increase the L/A ratio and hence the micro-heater resistance which results in lower power consumption and reduced voltage requirement. Interactive meshing (adjustable tetrahedral mesh) was used for simulating the micro-heater as a constant power source. The PCR droplet (10 μL)-to-micro-heater size ratio was also examined during the COMSOL simulations. Result of the multiphysics simulation for the final, micro-heater design is shown in Figure 1. The multiphysics simulation assisted in adjusting the micro-heater power requirement and accommodating the surface-to droplet body temperature difference in the designed and fabricated micro-devices.

[0053] Thermoresistive effect in thin, patterned metal films was utilized to create the RTD sensors, which were coupled with each micro-heater element to facilitate active monitoring and control of the thermal zones. The RTD sensor resistance is related to a given temperature, given by the following expression.

$$R_{RTD} = R_o(1 + \alpha_{RTD}\Delta T) \qquad (3)$$

In the above equation (Eqn. 3), R_{RTD} is the resistance of the RTD sensor at temperature T expressed in terms of degrees Celsius, α_{RTD} is the temperature coefficient of resistance and R_o is the resistance of the metal film measured at the same temperature at which α_{RTD} is valid. Eqn. 3 is a simplified form of the generic Callendar-van Deusen equation [29], and is highly linear in the temperature range of 0 °C to 100 °C.

[0054] A Fluorescence thermometry technique was used for standard calibration of the RTD sensor. This technique is widely used in microfluidic systems, for measuring fluidic body temperature using one-color ratiometric laser induced fluorescence (LIF) [30]. In this technique,

a dilute concentration (0.1 mM) of temperature sensitive 'Rhodamine B' dye, which has strong temperature dependent quantum efficiency, was placed in the temperature control zone and its fluorescence signal vs. temperature dependence was captured using a fixed gain photomultiplier tube (PMT). In order to account for set-up based variance during different experiments, the extracted fluorescence signal is normalized with a reference signal at a known temperature (e.g. room temperature, 25°C). By measuring changes in the normalized fluorescent intensity the fluid temperature can then be determined using the standard calibration curve with high spatial and temporal resolution, as illustrated in Figure 2.

[0055] The standard calibration curve was correlated to the RTD surface temperature measured using an external thermocouple probe for each of the designed and fabricated micro-devices to ensure the correct required temperature in the thermal control zones.

[0056] Dispensing, mixing and subsequent manipulations of PCR sample and reagent droplets were achieved using two popular electro-actuation methods, namely Droplet dielectrophoresis (D-DEP) [16, 17] and/or, Electrowetting (EW) [13, 14].

[0057] In EW based droplet actuation schemes, passivated metal electrodes patterned on silicon or, glass substrates are energized with external electric field, at low frequency (DC – 1 kHz), to alter the interfacial force equilibrium at the droplet-surface boundary [14]. The liquid contact angle (CA) and hence the shape of the sample droplet is henceforth affected by the change of force equilibrium which, with the assistance of suitably tailored electrode structures, can be utilized to transport individual droplets. Such EW droplet actuation schemes frequently make use of two patterned surfaces, separated by a gap which depends upon the size of droplets to be handled (see Figure 3(a)) [13]. In many conventional EW electrode architectures, the lower substrate consists of large arrays of co-planer square or rectangular shaped electrodes, which are controlled and switched using inter-digitized, programmable input [13, 14]. The top surface and the gap are utilized to facilitate a larger droplet deformation, which helps to reduce the droplet actuation voltage. The two surfaces, gap, electrode geometry and dielectric insulation are key components of modern EW based DMF, which can achieve droplet dispensing, mixing/splitting and extensive droplet transport of microliter to nanoliter sample volumes [14]. Single surface based EW schemes require relatively higher actuation voltages (> 100 V_{pp}) and/or, super hydrophobic surfaces, in order to induce the large contact angle change necessary for such EW

droplet actuations [31]. EW actuation schemes provide versatile droplet handling capabilities but are often restricted by the sequential, digital actuation, requiring active electrode switching and hence a complex electrode architecture and electrical control/switching system. Droplet transport and mixing/splitting processes are restricted by the droplet volume, viscosity, density and surface tension of the fluidic samples. EW microfluidic devices have found applications in implementing PCR based bio-assays [21], immunoassays [32, 33] and several other bio-combinatorial assays; however, conventional microfluidic devices still suffer from lack of parallelism, complex electrode architectures, the necessity for active switching and large electrode capacitances.

[0058] Dielectrophoresis (DEP) is another electrokinetic effect observed when a dielectric body is placed under the influence of an external, spatially non-uniform electric field [34]. In case of dielectric fluidic samples, the DEP electro-actuation method results in generation of pondermotive DEP body force which can be leveraged to create controlled deformation of the fluidic mass towards the regions of higher Electric field intensity. Such DEP fluidic manipulation can be used for rapid, ultrafine droplet dispensing (Liquid-DEP (L-DEP)) [15, 16, 35] or, subsequent droplet manipulation (Droplet-DEP or, D-DEP) [16, 17] by energizing a pair of coplanar metal electrodes, patterned on an insulated substrate, using AC voltage. Attributes of a typical D-DEP electrode structure and the mechanism of the D-DEP droplet actuation are shown in Figure 3(b). Both electrodes of the D-DEP electrode pair are shaped as interconnected, unidirectional herring-bone structures usually inclined at 45° angle. When the electrode pair is energized by a lower voltage (<100 Vpp) and frequency (30-100 Hz) AC signal, it induces periodic deformations of the droplet which is placed at one end of the D-DEP electrode (see Figure 3(b)). The herring-bone shape ensures that the electric field induced droplet deformation is unidirectional, causing a net shift in the center of mass (CM) of the droplet. The periodic deformation and droplet oscillation frequency is twice the applied AC signal frequency [16, 17], hence resulting in transport of the fluidic sample droplets.

[0059] Both the aforementioned droplet actuation methods benefit from the presence of a top surface which can help retain a large droplet CA during the entire actuation process. The micro-device reported in this work utilizes a nano-textured superhydrophobic surface [25], which yields a very high droplet CA (~ 155°), resulting in a more reliable and efficient handling of PCR sample/reagent droplets, compared to non-textured hydrophobic surfaces.

[0060] One particular method for fabricating the DMF device of the invention is discussed in Example 2 below. However, it should be appreciated that other microfluidic device fabrication methods can also be used by one skilled in the art to produce the microfluidic device of the invention. Moreover, one skilled in the art having read the present disclosure can readily modify various materials and/or processes to produce microfluidic devices of the invention. Accordingly, the scope of the invention includes all such variations as well as other microfluidic device fabrication methods known to one skilled in the art.

[0061] Additional objects, advantages, and novel features of this invention will become apparent to those skilled in the art upon examination of the following examples thereof, which are not intended to be limiting. In the Examples, procedures that are constructively reduced to practice are described in the present tense, and procedures that have been carried out in the laboratory are set forth in the past tense.

EXAMPLES

[0062] **EXAMPLE 1**

[0063] *Real-time RT-PCR assay*: Primer and probe sequences from previously reported real-time RT-PCR assays were used for the detection of influenza A [36] and influenza C [2]. Both assays target the matrix gene and result in the amplification of a 105 base pair product for influenza A and 64 base pair product for influenza C. In this experiment, a modification of previous influenza A detection protocol that was validated was used. Briefly, the experiment consisted of using the TaqMan® Fast Virus One-Step RT-PCR Master Mix. This master mix requires a smaller reaction volume (10 μL) and allows for faster thermal cycling. Amplification was performed by one-step RT-PCR using the TaqMan® Fast Virus One-Step RT-PCR Master Mix, 0.8 μM each of sense and antisense primers and 0.2 μM of the labeled probe (see Table 1). Five μl of in-vitro RNA was combined with 5 μl of the master mix. The reaction parameters are described in Table 2.

Table 1: Reagent concentration and volumes used to prepare the RT-PCR reaction mix.

Reagent	**Working Conc.**	**Sample volume (μl)**	**Final Conc.**
Taqman Fast Virus One-Step RT-PCR MMix	4x	2.5	1x
INFC-M-Forward primer	20 μM	0.4	0.8 μM
INFC-M-Reverse primer	20 μM	0.4	0.8 μM

INFC-M-Probe (FAM)	10 μM	0.2	0.2 μM
PCR Water	N/A	1.5	N/A
Master Mix Volume		**5.0**	

[0064] *Preparation of RNA transcripts*: Primers flanking the detection region were utilized to amplify fragments of the M gene including the region targeted by the primers and probes for the real-time assays from control strains. We used amplicons from Influenza A/Wyoming/03/2003 and Influenza C/Taylor/1233/47. The PCR products were cloned using the TOPO TA Cloning Dual Promoter Kit (Life Technologies, California, USA). The plasmid DNA was linearized using restriction enzymes Hind III and transcribed using the T7 RiboMAXTM Express (Promega, Madison, WI, USA) to synthesize negative-strand RNA in vitro. The transcribed RNA was spectrophotometrically quantified and serial dilutions were utilized for testing.

Table 2: Protocols for the chip based RT-PCR reactions.

Step	**RT reaction**	**Enzyme Activation**	**PCR (Cycles 30X)**	
			Denaturation	**Annealing (data acquisition)**
Temperature	50 °C	95 °C	95 °C	60 °C
Time	5 min	20 sec	3 sec	20 sec

[0065] The DMF devices were designed using MEMSPro L-Edit (v. 8.0) and the micro-heater component was optimized using COMSOL Multiphysics (v. 4.2). The optimized integrated microchips were fabricated at a micro/nano fabrication facility (Nanofab, Edmonton, Canada). The device fabrication procedure is outlined in Figure 4. The qRT-PCR micro-devices were fabricated on a 4" Borofloat substrate. It consisted of a pair of patterned metal (Cr) based micro-heater and resistance temperature detectors (RTDs) to create the two temperature control zones required for PCR thermal cycling, patterned gold/chrome overlay as electrical connectors for the resistive heaters/RTD sensors and one or two layers of patterned Aluminum or Au/Cr metallization for DMF electrode structures.

[0066] These metal layers were electrically isolated and passivated using dielectric stacks of silicon nitride (Si_3N_4), to prevent sample electrolysis. The top nitride layer is furthermore rendered super hydrophobic (SH) using a soft-lithography based nano-texturing technique, as reported in [25]. The nano-textured SH surface ensures a high droplet contact angle (CA ~ 156°) while significantly minimizes the extent of sample adsorption and the resulting loss of CA.

Advantage of such SH surfaces for DEP liquid actuation of TAQ DNA polymerase was studied in [25].

[0067] The experimental set-up utilized in this experiment is illustrated in Figure 5. It is comprised of a NI-PXIe-1062 (National Instruments, USA) system, used to control the microfluidic actuations as well as the on-chip thermal control units (TCUs). An isothermal plate (TOKAIHIT, Japan) is utilized to create and maintain a 50 °C base temperature during all operations. Fluorescent Microscope (Olympus BX-51) based optical set-up consists of: suitable excitation/emission filters, a high gain photomultiplier tube (Hamamatsu, Japan), color CCD camera (QImaging, Canada) and a high speed CMOS camera (Canadian Photonics Lab, Canada). The photomultiplier tube (PMT) is operated at a fixed, high gain ($x10^6$) for quantification of the fluorescence signal during chip based qRT-PCR assays. The DMF chip was secured on a printed circuit board (PCB), attached to an isothermal plate and mounted onto a motorized XY microscope stage for imaging and data acquisition. The electro-actuation of bio-fluids was accomplished using a waveform generator (TTi, USA) and a precision power amplifier (Fluke, USA) whereas; the TCUs were powered by a dual channel DC power supply (Power Designs Inc., USA).

[0068] Figure 5 also shows the microchip-PCB assembly on the isothermal plate. In order to minimize evaporation of the PCR sample during the thermal cycling process, the microfluidic chip was immersed in PCR-grade mineral oil (Biomerieux, Canada), encapsulated within a plexiglass fixture and an ITO coated glass cover, maintained at 50 °C during the qRT-PCR reactions. The presence of ITO coated heated top plate, to seal the mineral oil bath, resulted in reducing the evaporative and diffusion based sample volume loss to less than 10 % of the reaction volume. The two integrated micro-electrode architectures used for the chip based qRT-PCR reactions are illustrated in Figure 6. The microfluidic component in each structure consists of three sections: 1) dispensing and mixing section where the RNA sample droplet and PCR reagent droplet is mixed; 2) transport section which is maintained at 50 °C for the RT-reaction and subsequently transports the PCR droplet onto the thermal cycler section; 3) the third section is the on-chip PCR thermal cycler design which has two TCUs (maintained respectively at 65 °C and 95 °C) and a D-DEP electrode scheme to circulate the droplet between the two TCUs during the course of the qRT-PCR reaction. Micro-electrode 1 solely relies on D-DEP actuation for

sample/reagent dispensing to thermo-cycling, with two metalized layers (Al) of herring-bone shaped D-DEP electrodes, separated by ~ 300 nm of Si_3N_4 (see Figure 6). Micro-electrode 2 consists of single surface EW electrode array (Au/Cr) for dispensing, PCR sample/reagent mixing (electrode gap: 100 μm) and a linear, bi-directional D-DEP electrode scheme (Al) for PCR thermal cycling (Figure 6). Electrode pitch, gap and width for the mixing (pitch: 250 μm; gap: 50 μm) and transport (pitch: 300 μm; gap: 60 μm) micro-electrodes were optimized for 5μL and 10 μL droplet volumes respectively. Average droplet actuation speeds during the chip based qRT-PCR assays were found to be ~ 3 mm/sec.

[0069] During the qRT-PCR process, Fluorescence emission from the PCR droplet was captured for each cycle, during the annealing phase (at 60°C in TCU 2 zone), using the PMT based optical set-up. This captured fluorescence signal was plotted in real-time, with respect to cycling number to generate standard PCR curves. A logarithmic plot of the qRT-PCR curve yields a better observation of the very distinct reaction kinetics during the amplification process. *Ct* (threshold cycle) is defined as the intersection between an amplification curve and a threshold line, placed in the qRT-PCR curves above the signal noise floor. It can be shown to be related to the initial target concentration, in the PCR reaction. The equations below describe the exponential amplification of PCR:

$$N_n = N_i(1 + E)^n \quad (4)$$

Where, N_i = initial copy number; N_n = copy number at cycle n; n = number of cycles and E = efficiency of target amplification, with theoretical values between 0 and 1. When the reaction efficiency is a maximum (E = 1), the equation reduces to: $N_n = N_i(2^n)$ and the target DNA copy count increase by 2-fold at each cycle. The quantity of PCR product generated at each cycle decreases with decreasing efficiency, and the amplification plot is delayed. The measured efficiency (%) for successful and reliable PCR amplification should lie between 90 and 110%.

[0070] *Results and Discussion*: Experiments were conducted using the chip based qRT-PCR. The DMF device of the invention was used to perform qRT-PCR amplification of both influenza A and C virus RNAs. Limit of detection (LOD) of the qRT-PCR assays were determined and the device performance compared to that of the conventional qRT-PCR equipment. All chip-based qRT-PCR reactions, unless indicated otherwise, were carried out

using a recommended 10 μL PCR reaction volume in order to use the PCR reagent mixture in the same sample-to-reagent ratios, which were optimized for the conventional qRT-PCR set-up.

[0071] The two qRT-PCR micro-devices were first tested for amplification and detection of in-vitro synthesized RNA segment of the M-gene, of the influenza C virus. Mixing of the influenza C RNA sample and the off-chip prepared PCR reagents, followed by the RT reaction and thermal cycling over Micro-electrode 1, is shown in Figure 7. The first phase of droplet actuation combines the RNA sample droplet with PCR Master Mix. The mixed PCR droplet is then maintained at 50 °C for 5 minutes, to complete the RT-reaction (conversion of RNA to c-DNA) (see Figure 7). Once this stage is completed, the PCR droplet (volume: 10 μL) is conveyed onto the thermal cycler electrode, where it is subjected to 30-35 thermal cycles between the desired temperature set-points. In every cycle, fluorescent signal read-out is carried out during the annealing phase, at 60 °C (Figure 7). This droplet transport based thermal cycling is carried out in approximately 45 sec per PCR cycle and the entire process (dispensing to qRT-PCR amplification for 30 cycles) is completed within 30-35 minutes. The elapsed qRT-PCR process time for the micro-device is comparable to the conventional, fast qRT-PCR set-up from Applied Biosystems (ABI 7500).

[0072] The micro-graphs in Figure 8 illustrate the various reaction stages of chip based qRT-PCR assay, over micro-electrode 2. As reported earlier, this electrode design incorporates single surface EW for mixing of influenza C RNA and the PCR reagent mix (see Figure 8). The mixed PCR droplet (volume: 10 μL) is subsequently transferred onto a linear, bi-direction D-DEP electrode design where it is initially held at 50 °C for RT reaction. The droplet is then cycled over the two TCUs maintained at the desired temperatures and PMT read-out is again carried out during the annealing phase (see Figure 8). Each thermal cycle over this electrode design was accomplished in 35 seconds. This results in a complete qRT-PCR assay (30 PCR cycles) within 30 minutes. The quantitative PCR curves extracted for amplification of influenza C virus over micro-electrode 1 structure is reported in Figure 9.

[0073] The stock influenza C RNA sample (C1: 4510 copies per 5 μL) was sequentially diluted to create four samples with an order of magnitude difference in their RNA concentration. The four samples (C1, C2, C3 and C4) where then actuated over micro-electrode 1 and the raw qRT-PCR data was extracted, as shown in Figure 9. The PMT photocurrent, which is

proportional to the fluorescence signal, was used to extract the logarithmic plot of PCR cycle vs. PMT output. The threshold signal level was manually placed based on the signal noise levels before the amplification starts. The threshold level was set at the onset of exponential amplification region of the extracted quantitative PCR curves. C_t was then extracted as the PCR cycle number just above the threshold signal level (second cycle in the exponential amplification region). The extracted C_t values, along with the qRT-PCR curves for the four influenza C samples are reported in Figure 9. The lowest RNA concentration subjected to the chip based qRT-PCR detection was quantified as ~ 5 viral RNA copies per PCR reaction.

[0074] Efficiency of the chip based qRT-PCR reaction, extracted using Eqn. 4, and was found to be ~ 96.5 %. The acceptable qRT-PCR efficiency confirms the reliability of the developed micro-device for on-chip qRT-PCR detection assays.

[0075] Once the influenza C RNA was successfully detected using the qRT-PCR micro-device, it was used for amplification and detection of in-vitro synthesized M-gene RNA of the influenza A virus. The stock RNA solution (A-1; conc.: 2930 copies per 5 μL) was again sequentially diluted to achieve three orders of magnitude variation in the initial RNA concentration.

[0076] The four influenza A RNA samples (A-1, A-2, A-3 and A-4), along with a negative control sample, were actuated utilizing micro-electrode 2. The extracted qRT-PCR curves from two different sets of chip based qRT-PCR reactions are reported in Figure 10. In order to confirm the detection of influenza A RNA in the ultra-low concentration sample, A-4, four identical A-4 samples were prepared off-chip and qRT-PCR amplified over different micro-devices. Two out of the four A-4 samples (~ 3 copies per PCR volume) were successfully amplified and detected whereas the other two yielded in no detectable amplification over the 35 PCR cycles, as reported in Figure 10. The 50% sensitivity of detection at the lowest RNA concentration in sample A-4 could be a result of off-chip sample preparation. Efficiency of the qRT-PCR amplification, for each of the four influenza A sample was found to be ~ 94.4 %.

[0077] Quantitative PCR exploits the linear relationship between C_t and the logarithm of the number of initial copies N_i of the template, which is predicted from Eqn. 4. Figure 11 shows that the data obtained with influenza A and influenza C RNA templates is in conformity with the

predicted behavior of the quantitative PCR. From Eqn. 4 the slope m of this linear curve can be shown to be related to the efficiency E as follows:

$$E = 10^{-1/m} - 1 \qquad (5)$$

The slope was calculated from the experimental data by linear regression and the measured efficiency is then derived from Eqn. 5. For the qRT-PCR data of influenza C, the slope was found to be: -3.4, corresponding to PCR efficiency of 97% whereas for influenza A qRT-PCR experimental data, the slope was estimated to be: -3.46, which corresponds to a PCR efficiency of 95%.

[0078] The LOD for the chip based qRT-PCR assay is calculated to be ~ 5 viral RNA copies per PCR reaction. It should be noted that at such low sample concentrations, manual sample preparation can influence the detection threshold. As a demonstration of principle these experiments establish a performance level comparable to standard PCR methodologies.

[0079] The qRT-PCR experiments described herein used 10 μL volume PCR droplets to achieve a droplet transport based qRT-PCR reaction. The PCR volume was maintained constant in order to compare micro-device performance with the conventional, off-chip PCR set-up which requires a minimum of 10 μL PCR reaction volume. One of the advantages of DMF devices of the invention is substantial reduction in the required bio-sample/reagent volumes. Results of different volume (1 μL, 2.5 μL, 5 μL, 7.5 μL and 10 μL) qRT-PCR experiment are reported in Figure 12. The different volume PCR droplets were all pipetted from a 40 μL PCR reaction mix (20 μL influenza C RNA sample + 20 μL PCR Master Mix™). The 7.5 μL and 10 μL PCR droplets were successfully actuated over micro-electrodes 1 and 2 respectively to achieve transport based PCR reaction. However, due to the fact that the two micro-electrode structures were tailored for PCR volumes close to 10 μL, PCR droplets < 5 μL were subjected to a static PCR thermal cycling, where they were positioned in each one of the two TCUs and the thermal zones were cycled between the two temperature limits of 60 °C and 95 °C. Cycle time for static qRT-PCR was observed to be 2.5 times larger than that of transport based PCR assay. As a result of the slower ramp rates, the PCR droplet is exposed in the high temperature region (between 80 °C – 95 °C) for a larger amount of time, per cycle during the entire qRT-PCR reaction. This coupled with the smaller droplet volumes, resulted in change in the PCR efficiency for the smaller 2.5 μL PCR droplet (see Figure 12). Furthermore, the 1 μL PCR droplet did not show

any amplification and suffered from significant volume loss (>25% of sample volume was lost during the first 10 cycles). The PCR efficiency for the 7.5 μL and 10 μL PCR droplets was close to ~ 95%; whereas the efficiencies of the 5 μL and 2.5 μL PCR were found to be ~ 90 % and 78%, respectively. The calculated PCR efficiency values indicate that the transport based chip qRT-PCR is superior to the static PCR method. The poor performance of PCR in the smaller reaction volumes can henceforth be attributed to the fact that the current experimental set-up and the micro-electrode structures were tailored to handle larger PCR droplets (close to 10 μL); however, this exercise does demonstrate the possibility of reducing the PCR reaction volumes to microliter or sub-microliter PCR droplets. Although from the view-point of clinical pathogen detection, the possible reduction of PCR droplet volumes is not a significant improvement since the point of emphasis for such applications is to lower the detection threshold which may often require sampling larger sample volumes for the qRT-PCR detection assays.

[0080] Some aspects of the invention provide integrated droplet microfluidic devices. In some embodiments, DMF devices of the invention include a nano-textured superhydrophobic top surface that is capable of electro-handling of droplets. DMF devices of the invention facilitate chip based mixing/sample preparation and chip based qRT-PCR amplification. In some embodiments, devices of the invention can be used in clinical diagnostic assays, e.g., detection of influenza viruses as well as other clinical diagnostic assays. Some DMF devices of the invention can include multiplexed qRT-PCR chips that can be used, for example, for clinical experimentation, where numerous repeated testing of known and unknown viral samples is required to provide robust pathogenic bio-diagnostics.

[0081] **EXAMPLE 2**

[0082] *Device Fabrication*: The DMF device is micro-fabricated using patterned metal, dielectric layers and nano-roughened top surface coating, all housed on a passivated silicon substrate (see Fig. 13). Since fabrication methods for such devices have been reported previously (see, for example, Kaler et al., *Biomicrofluidics*, **2010**, *4(2)*, 1–17), this section focuses on a process for creating the nano-textured super hydrophobic ("SH") surface. Several techniques have been proposed to create patterned micro/nano-roughened surfaces which can achieve liquid contact angles in the extremely wide range of ~10–170°.

[0083] However, for DMF devices, the goal is to achieve large droplet contact angles ("CAs") (e.g., 140–160◦). Some processes of DMF fabrication include colloidal lithography (see, for example, Egitto, *Pure and Applied Chemistry*, **1990**, *62(9)*, 1699–1708), where colloidal nano-particles are spin/dip coated on the chip surface to form mono-dispersed, hexagonally close packed assembly of spheres (Fig. 14(a)). Briefly, PS nanospheres (diameter: 450 nm; 1% solid), purchased from Corpuscular Inc., USA, were suspended in a solvent mixture of 1 part Triton X-100 and 400 parts methanol (95% pure). The bead sample to solvent ratio in the final dispersion was kept at 7:1 (volume ratio), finalized iteratively to ensure mono-dispersed deposition of nano-spheres, as shown in Fig. 14(a).

[0084] Oxygen plasma based reactive ion-etching process was then used to shrink the nano-spheres up to diameter 150–200 nm and hence a solid fraction (ϕ_s) was created at the surface. Once the nanospheres were optimally shrunk, they acted as nano-imprint for the next step which was to etch the exposed Si_3N_4 layer using C_4F_8 plasma, creating nano-posts with diameter ~150–200 nm. As illustrated in Figs. 13 and 14(b) and (c), generated roughness parameter (ϕ_s) was related to the initial diameter (d_{po}). The polystyrene cover from top of the nano-posts was removed by ultra-sonication in acetone for 30–40 min. Figs. 14(d) and (e), respectively, show the short range (over a 5 μm x 5 μm area) and long range (over a 20 μm x 20 μm area) uniformity of the generated nano-pattern. Figs. 4(f) and (g) show a tilted (70°) SEM view of the nano-patterns. Since the generated Si_3N_4 nano-roughness is super-hydrophilic by nature, approximately 45–50 nm of composite fluorocarbon (FC) layer, consisting of 25 nm of plasma deposited FC and ~25 nm of spin coated TEFLON® AF 1600 resin (DuPont USA) was deposited on top of the nano-roughened surface, as shown in Figs. 14(h) and (i). Nano-post height (h_p) and solid fraction (ϕ_s) were optimized experimentally using an array of fabricated aspect ratios to produce the highest CA and low contact angle hysteresis (CAH). Table 2-1 below shows the range of post dimensions fabricated and tested highlighting some of the representative dimension range. CA was measured using a GBXDIGIDROP set-up at ambient atmospheric conditions (temperature ~25 °C and humidity ~40%) in the static and dynamic mode. CAH was calculated as the difference between the receding and the advancing CA. Typical CA measurements were conducted by dispensing five different sessile deionized ("DI") water drops (5 mL), dispensed at 0.5–1 mLs^{-1} on the patterned devices, to examine the static CA and the

CAH for the advancing/receding droplet boundary. Based on the five repeated measurements on each sample device, the mean CA and CAH values are reported in Table 2-1. The standard deviation for the reported measurements, based on the accuracy of the measurement process and the pattern uniformity on the samples was found to be of the order of $\pm 2°$. Experimental and modeling results were generated using the selected nano-structures, highlighted in Table 2-1. Three CA measurements are reported in Fig. 15, comparing CA on a composite FC coated (Fig. 15(a)) surface and two nano-patterned test structures (Figs. 15(b) and (c)).

Table 2-1: Aspect ratio and contact angle/hysteresis data for fabricated nano-structures.

Height (h_p in nm)	Solid fraction (ϕ_s)	0.15	0.20	0.30	0.38	0.51	0.68
80	Contact angle (CA)/ Contact angle hysteresis (CAH) matrix	145°/ 19°	144°/ 18°	140°/ 15°	135°/ 19°	129°/ 16°	121°/ 20°
100		154°/ 10°	150°/ 12°	144°/ 10°	141°/ 14°	129°/ 16°	124°/ 18°
150		156°/ 9°	152°/ 10°	146°/ 8°	143°/ 9°	135°/ 6°	128°/ 16°
180		156°/ 10°	153°/ 9°	148°/ 7°	144°/ 10°	136°/ 8°	128°/ 12°
200		155°/ 12°	152°/ 15°	147°/ 12°	144°/ 12°	136°/ 13°	128°/ 12°

[0085] *Sample preparation and experimentation*: The performance of LDEP based SMF devices in the SH regime, (CA > 140◦), was investigated. Using the fabrication process disclosed herein, DMFs having CAs in the range of 150–160° were produced. In order to observe both the hydrophobic and SH regime (e.g., CA between 90° and 160°), various concentrations of non-ionic surfactant were utilized, e.g., Tween-20, which resulted in lowering of the interfacial surface tension and the resultant contact angle; between 135° and155° on the SH surface and between 95° and 115° on the hydrophobic surface. The used concentrations and the resultant CA, surface tension values are reported in Table 2-2 below.

Table 2-2: Concentration and interfacial properties of used Tween-DI water solutions.

Sample number	Conc. (% by vol.) of Tween-DI	Contact angle (°) (Teflon™)[a]	Contact angle (°) (patterned)[b]	Surface Tension (dyne/cm)[a]
1	0 (pure DI)	115	154	72.8
2	0.00001	102	148	71.4
3	0.0001	94	145	65.7
4	0.001	79	140	51.6
5	0.005	75	138	44
6	0.01	72	136	32.6
7	0.1	65	135	30.4

a. CA over TEFLON® and surface tension values are from Singh et al., JAOCS, **1984**, *61(3)*, 596–600.
b. CAs over patterned surface are reported as mean values of 5 measurements, with a standard deviation of +/- 2°.

[0086] The shaded cells in Table 2-2 represent the experimental conditions used while analyzing the effect of CA on the static and dynamic characteristics of LDEP actuations. TAQ DNA polymerase enzyme was purchased from Invitrogen, USA (M.W. – 94 kDa; stock conc: 5 U/μL). TAQ sample used in the reported experiments were diluted up to PCR concentrations with a non-ionic TRIS-MES buffer (pH ~7.8), and the used sample conc. was ~0.35 mg/mL.

[0087] An opto-electronic setup was used to perform the experiments. Thus, the SMF chip was secured using spring-loaded pogo pins onto a PCB for external electrical connections. The chip-PCB arrangement was secured on a fluorescent microscope platform (BX51, Olympus, Japan) which was set-up with a high speed CMOS imager (Mega speed) and a CCD color camera (QImaging, Canada) to record the dynamics of LDEP actuation and dispensing of enzyme/macromolecule samples. A signal generator (TGA1244, TTi, UK) and a high-voltage, high-frequency power amplifier (Precision Power Amplifier 5205A, Fluke) were used to generate the AC voltage needed to drive the coplanar electrode arrangement. The actuation process was controlled using a LabVIEW (NI LabVIEW, USA) software driver and the output data was recorded either in form of high speed videos (original frame rates: 2000–2500 fps) using the high speed camera. The high speed videos were digitized and analyzed using an image probing software (provided by Mega speed). An absorption spectroscope (Nanodrop 2.0) was used to analyze and measure the TAQ concentration during the experiments.

[0088] The LDEP actuations on electrode schemes, shown in Fig. 13, were conducted by energizing the electrode pair using a 200–450 Vpp AC voltage at a frequency of 100 kHz. The actuations were conducted both in air and under 5 cSt silicone oil bath.

[0089] *Results and discussion*: The behavior of LDEP actuation on SH surface is significantly different to that of a regular hydrophobic surface. This difference in behavior of LDEP actuation on SH was validated by experimental data, which was obtained using various aqueous samples. Furthermore, the performance of LDEP actuation of homogeneous aqueous samples (Table 2), as well as complex samples containing TAQ enzyme, were observed for the SH surface and were compared to the data obtained using a non-textured hydrophobic coatings (θ_e ~116°).

[0090] *Threshold actuation voltage*: Based on the model predictions, the threshold voltage for LDEP actuation on SH surface is expected to be higher than that for smooth hydrophobic surfaces. This is due to the increase in the fluidic surface energy at higher CAs and the increased surface tension force. Tween-DI solutions, reported in Table 2-2, were actuated on both hydrophobic (CA ~116°) and SH surface (CA ~156°), over LDEP electrode (w = g = 20 μm). The liquid CA was controlled by altering the Tween concentration. CA was varied from 95° to 156° (Table 2-2). The experimental threshold voltage (V_{th}) was determined by actuating the liquid sample and reducing the actuation voltage up to a minimum value (V_{min}) such that the parent is distorted enough to create a marginal liquid protrusion, as shown in Fig. 16(b). Figs. 16(a) and (c) shows the experimental values of V_{th} (V_{min}), reported as mean values based on 10 repeated actuations (standard deviation: 5 V), plotted alongside the theoretical data to demonstrate the accuracy and scalability of the LDEP actuation for SH surfaces. The theoretical data was estimated using the static analysis of the lumped model. For all LDEP actuations reported in Fig. 16, the model successfully accounted for the combined effect of change in liquid surface tension (γ) and CA.

[0091] *Dynamics of LDEP actuation over hydrophobic and SH surfaces*: The dynamics of LDEP liquid actuation was studied for at least two principle reasons: (1) to confirm that the model can successfully account for the transient behavior of LDEP actuation and, (2) to ensure that the SH surface does not adversely impact jet break-up and dispensing of sample/reagent droplets upon removal of the applied voltage. The Tween-DI samples were actuated over the

LDEP electrode structure, with both hydrophobic and SH top coatings. The experimental data for the composite coated hydrophobic and the SH surface was extracted and plotted alongside the theoretical curves (Fig. 17), generated using the developed model. Figs. 17(a) and (b) show dynamics of liquid actuation over hydrophobic surface whereas Figs. 17(c) and (d) report liquid actuations over the SH surface. The experimental dataset (z vs. t) plotted in Fig. 17 is the mean value of the actuated jet lengths (z), estimated over 10 LDEP actuations for each liquid sample, with a standard deviation of 70 μm, reported as error bars in the individual plots (see Fig. 17). The four micrographs in Fig. 17 confirm that the model accurately accounts for the various Tween- DI sample actuations, varying in both CA and surface tension, as shown in Table 2-2. The results furthermore show that the actuation velocities (both maximum and average) are higher for the SH surface, barring the fact that the actuation voltages are adjusted based on the effective dielectric layer, on top of the electrode structure (see Fig. 18). Another interesting observation from Fig. 17 is the profile of the reported LDEP actuation dynamics. LDEP actuations in the hydrophobic regime (CA ~95–115°) were found to exhibit $z \propto t^{1/2}$ behavior (Fig. 17(b)). However, as evident from Fig. 17(d), the various LDEP actuation dynamics show a complex z vs. t profile, up to ~15 ms. Without being bound by any theory, it is believed that this actuation time period is comparable to the characteristic time constant (Tμs) and thus contains significant contributions from both the viscous and inertia dominant domains. As a result, the plots in Figs. 17(c) and (d) show contributions from both z ($\propto$ t, $t^{1/2}$) behavior up until ~15–20 ms of actuation time, unlike the hydrophobic liquid jet actuations (Figs. 17(a) and (b)), where the dynamics is strongly controlled by $t^{1/2}$ and the viscous component. This observation is consistent with the finding that the general solution, comprising of both the inertia ($z \propto t$) and viscosity ($z \propto t^{1/2}$) dominant time scales are involved during the LDEP actuation over SH surfaces.

[0092] *Jet break-up and droplet dispensing*: One of the crucial phases during the LDEP based rapid droplet dispensing process is the destabilization and break-up of the liquid jet, upon removal of the actuation voltage. The breakup of the liquid jet is believed to be influenced by at least in part both the device surface and the fluidic properties. It has been shown that for non-uniform and more hydrophilic surfaces, disintegration of the liquid jet is slower and more uncontrolled as compared to a hydrophobic surface with less friction.

[0093] Figs. 19(a)–(c) shows disintegration of liquid jet on a composite coated hydrophobic surface where within few actuations (sometimes even during the 1st actuation), jet break-up is believed to be affected by the surface irregularities. In contrast, over SH surface with nano-patterns, the disintegration of liquid jet is found to be relatively faster (<0.25 ms) and more reliable as compared to a smooth hydrophobic surface (1.5–2 ms) (Figs. 19(d)–(f)). This is believed to be a direct consequence of the minimized surface friction (the slip boundary at the surface) and the increased capillary instability due to the increased capillary pressure on the formed liquid jet. As a result, dispensed droplet volumes along large LDEP electrode lengths have been found to be even more uniform for the SH surface. From Fig. 19(c), one can also observe the formation of ultrafine satellite droplets, away from the droplet collection sites in the case of the hydrophobic surface which were not observed for SH surfaces (Fig. 19(f)). Thus, SH surfaces are superior to a hydrophobic surface to minimize formation of satellite droplets and facilitate uniform sample/reagent droplet dispensing over longer electrode lengths.

[0094] *Advantages of LDEP on SH surface for manipulating enzymes and macro-molecules*: As disclosed herein, the present inventors have established that SH surfaces are capable of reproducible and controlled LDEP actuation and subsequent droplet dispensing. However, it remains to be seen whether the developed SH surface can minimize extensive loss of droplet CA and surface adsorption of macro-molecules. Both these features are essential if the SH LDEP devices are to be leveraged for on-chip bio-assay where large concentration of enzymes, are often encountered during chip based RT-PCR assays or post-amplification detection/screening assays. An optimum SH surface will reduce the requirement for off-chip sample preparation/handling steps such as washing, dilution, buffer exchange.

[0095] To this end, performance of LDEP actuation on the developed SH surface was investigated for a macro-molecule, which is used extensively in today's bio-diagnostic applications. TAQ-DNA polymerase is a key ingredient of nearly every PCR, rt-PCR and RT-PCR based bio-detection and it's a highly active enzyme that has been shown to instantly adsorb to hydrophobic coatings such as TEFLON®. However, as shown in Fig. 20 for the composite FC surfaces, adsorption was contained to within the first few seconds of exposure, resulting in an instantaneous drop in liquid CA (~60°). Without being bound by any theory, it is believed that the reason nano-patterned SH surface can minimize the adsorption and the resultant drop in CA

is based on the restricted exposure of solid–liquid interface and the relatively high initial CA, so long as the sample droplet retains the Cassie-Baxter profile. Figs. 20(a) and (b) show the superior performance of the SH surface where the sample adsorption, measured at the parent droplet site in between repeated LDEP actuations (six LDEP actuations, each at an interval of 60 s), is reduced by up to 20% (see Fig. 20(a)) as measured using the spectrophotometer. The loss in droplet CA, in both parent droplet (measured using a goniometer) and the dispensed daughter droplets (analyzed experimentally by measuring the droplet radii of six-eight dispensed droplets on the SH surface), was reduced from 48% to 11.5% of the initial CA over six LDEP actuations, as shown in Fig. 20(b). No further loss of droplet CA was observed in subsequent LDEP actuations which were repeated up to 15 LDEP actuations utilizing the same electrode structure.

[0096] Fig. 21 shows actuation of aqueous TAQ sample (concentration: 0.35 mg/mL) on a standard hydrophobic surface. During the first actuation (Fig. 21(a)), a sluggish jet actuation was observed (even at $V_a > V_{th}$), as confirmed by the profile of the advancing liquid jet. However, since the LDEP actuation and subsequent jet break-up is a very rapid process (~15–20 ms), jet break-up and resulting nL droplet formation was achieved during the first actuation (Fig. 21(b)) although, the dispensed droplets were poorly shaped due the lowered CA and surface adsorption (Fig. 21(b)). The subsequent actuations resulted in an uncontrolled jet breakup and due to the increased wettability the jet doesn't disintegrate completely, leaving a liquid trench rather than a droplet array (Figs. 21(c)–(f)). The adsorption was analytically confirmed by measuring the TAQ conc. in the parent droplet after every minute, as reported in Fig. 20.

[0097] Similar experiments were then conducted on the SH surface (CA ~156°). Fig. 22 shows the second LDEP actuation over the same LDEP electrode pair, which resulted in a more uniform liquid jet and subsequent rapid dispensing (~20 s) of 300 pL TAQ enzyme daughter droplet array which were spherically shaped with CA ~138°, as shown in Fig. 22. Similar actuation and dispensing results were obtained for the 4–5 repetitions of TAQ enzyme actuation over the SH surface. The change in TAQ conc. in the parent droplet further validates the reduced surface adsorption and a relatively small drop in the parent TAQ CA (reported in Fig. 20).

[0098] The experimental observations confirmed that the developed SH surfaces are highly suitable for actuation of TAQ DNA polymerase and other similar macro-molecules. The resulting high CA of TAQ droplets on these SH surface is favorable for subsequent droplet

manipulations (transport, mixing, thermal cycling), required in order to conduct on-chip PCR based bio-assays.

[0099] *Conclusions*: In this example, the performance of SH surfaces for LDEP liquid actuations was analyzed. An electro-fluid-mechanical lumped model was developed to improve upon the existing lumped model such that the effects of CA variation over a large range (hydrophobic to superhydrophobic) and the influence of nano-textured, periodic surface roughness can be evaluated. Experimental findings were compared to the developed model to validate the theory and establish that LDEP actuation on SH surfaces have significant benefits in terms of faster yet more controlled liquid actuation and dispensing speeds (for rapid screening). The example also demonstrates a far superior handling of PCR grade TAQ DNA polymerase enzyme during the LDEP actuation and dispensing process, using the nano-patterned SH surface. The nano-patterned SH surface can also be used for post-amplification pathogen screening assay, where conventional microfluidic devices have been restricted by the large enzyme concentrations, which were difficult to manoeuver over ordinary hydrophobic surfaces.

[0100] **References**

1. P. F. Wright, G. Neumann and Y. Kawaoka, Orthomyxoviruses. Fields Virology: Chapter 41, 6th ed, Knipe D. M., Howley P.M. eds, Lippincott Williams & Wilkins, Philadelphia (2013).
2. K. Pabbaraju, S. Wong, A. Wong, J. May-Hadford, R. Tellier and K. Fonseca, *Influenza Other Resp Viruses*, doi: 10.1111/irv.12099 (2013).
3. K. Mullis, F. Faloona, S. Scharf, R. Saiki, G. Horn, H. Erlich, Specific Enzymatic Amplification of DNA In Vitro: The Polymerase Chain Reaction, *Cold Spring Harb Symp Quant Biol.*, **51(1)**, 263-73 (1986).
4. R. K. Saiki, D. H. Gelfand, S. Stoffel, S. J. Scharf, R. Higuchi, G. T. , Horn, K. B. Mullis and H. A. Erlich, *Science*, **239**, 488-491 (1988).
5. A. Betts Carpenter, Immunoassays for the Diagnosis of Infectious Diseases. Chapter 5: pp 60-72, Manual of Clinical Microbiology 10th ed., ASM Press Washington DC (2011).
6. C. T. Wittmer and N. Kusukawa, Real-time PCR and melting analysis, Molecular Microbiology Diagnostic Principles and Practice: Chapter 4, 2nd ed Persing DH ed, ASM Press Washington (2011).
7. V. Datta and R. T. Hayden, In vitro nucleic acid amplification techniques, Molecular Microbiology Diagnostic Principles and Practice: Chapter 3, 2nd ed Persing DH ed, ASM Press Washington (2011).
8. K. Pabbaraju, S. Wong, B. Lee, R. Tellier, K. Fonseca, M. Louie and S. J. Drews, *Influenza Other Resp Viruses*, **5(2)**, 99-103 (2011).

9. R. Prakash, K. V. I. S. Kaler, D. P. Papageorgiou, A. G. Papathanasiou and R. Tellier, *Proc. 8th International meeting on Electrowetting*, Athens (2012).
10. E. T. Lagally, C. A. Emrich and R. A. Mathies, *Lab Chip*, **1-2**, 102–107 (2001).
11. I. Erill, S. Campoy, N. Erill, J. Barbe and J. Aguilo, *Sens. Act. B: Chem.*, **96(3)**, 685–692 (2003).
12. R. A. Mathies and E. T. Lagally, *J. Phys. D: Appl. Phys.*, **37**, R245–R261 (2004).
13. M. G. Pollack, A. D. Shenderov and R. B. Fair, *Lab Chip.*, **2(2)**, 96–101 (2002).
14. F. Mugele and J. C. Baret, *J. Phys.: Condens. Matter*, **17,** R705–R774 (2005).
15. T. B. Jones, *J. Electrostatics*, **51**, 290–299 (2001).
16. K. V. I. S. Kaler, R. Prakash and D. Chugh, *Biomicrofluidics*, **4(2)**, 022805 (2010).
17. M. Gunji, H. Nakanishi and M. Washizu, *Proceedings of Micro Total Analysis Systems*, **1**, 168–170, 2004.
18. M. Hashimoto, P. C. Chen, M. W. Mitchell, D. E. Nikitopoulos, S. A. Soper and M. C. Murphy, *Lab Chip*, **4**, 638–645 (2004).
19. E. T. Lagally *et. al.*, *J. Anal. Chem.*, **76**, 3162–3170 (2004).
20. R. H. Liu, J. N. Yang, R. Lenigk, J. Bonanno and P. Grodzinski, *J. Anal. Chem.*, **76(7)**, 1824–1831 (2004).
21. M. G. Pollack, A. D. Shenderov and R. B. Fair, *Proc.* μ*TAS 2003*, California, USA (2003).
22. R. Tewhey *et. al.*, *Nature Biotechnology*, **27**, 1025-1031 (2009).
23. E. T. Lagally, P. C. Simpson and R. A. Mathies, *Sensors and Actuators B*, **63(3)**, 138-146 (2006).
24. R. Zhong, X. Pan, L. Jiang, Z. Dai, J. Qin and B. Lin, *Electrophoresis*, **30**, 1297-1305 (2009).
25. R. Prakash, D. P. Papageorgiou, A. G. Papathanasiou and K. V. I. S. Kaler, *Sensors and Actuators B: Chemical*, **182**, 351-361 (2013).
26. M. G. Roper, C. J. Easley, L. A. Legendre, J. A. Humphrey and J. P. Landers, *Anal. Chem.*, **79(4)**, 1294-1300 (2007).
27. H. Kim, S. Dixit, C. J. Green, G. W. Faris, *Opt. Express*, **17(1)**, 218-227 (2009).
28. J. Khandurina, T. E. McKnight, S. C. Jacobson, L. C. Waters, R. S. Foote and J. M. Ramsey, *Anal. Chem.*, **72**, 2995-3000 (2000).
29. T. D. McGee, Principles and Methods of Temperature Measurement, ISBN: 978-0-471-62767-8, John Wiley and Sons, New York (1988).
30. T. Glawdel, Z. Almutairi, S. Wang and C. Ren, *Lab Chip*, **9(1)**, 171-175 (2009).
31. J. Heikenfeld and M. Dhindsa, *Journal of Adhesion Science and Technology*, **22**, 319-334 (2008).
32. E. M. Miller, A. H. C. Ng, U. Uddayasankar and A. R. Wheeler, *Anal. Bioanal. Chem.*, **399**, 337-345 (2011).
33. V. Sivagnanam *et. al.*, *J. Anal. Chem.*, **81**, 6509–6515 (2009).
34. H. A. Pohl, *J. Appl. Phys.*, **29(8)**, 1182 – 1188 (1958).

35. T. B. Jones, M. Gunji, M. Washizu and M. J. Feldman, *J. Appl. Phys,* **89(3)**, 1–8, 2001.

36. F. S. Dawood, L. Finelli, M. W. Shaw *et. al.*, *N. Engl. J. Med.,* **360**, 2605–2615 (2009).

[0101] The foregoing discussion of the invention has been presented for purposes of illustration and description. The foregoing is not intended to limit the invention to the form or forms disclosed herein. Although the description of the invention has included description of one or more embodiments and certain variations and modifications, other variations and modifications are within the scope of the invention, e.g., as may be within the skill and knowledge of those in the art, after understanding the present disclosure. It is intended to obtain rights which include alternative embodiments to the extent permitted, including alternate, interchangeable and/or equivalent structures, functions, ranges or steps to those claimed, whether or not such alternate, interchangeable and/or equivalent structures, functions, ranges or steps are disclosed herein, and without intending to publicly dedicate any patentable subject matter.

What is Claimed is:

1. A droplet-based microfluidic device comprising:

a substrate having a surface;

a plurality of micro-electrodes patterned on said surface, wherein said plurality of micro-electrodes are configured to confine, electrically actuate and transport liquid droplets; and

a passivating surface coated onto said plurality of micro-electrodes, wherein said passivating surface comprises a superhydrophobic material.

2. The droplet-based microfluidic device of Claim 1, wherein said passivating surface is nano-textured.

3. The droplet-based microfluidic device of Claim 2, wherein said nano-textured superhydrophobic material is adapted to prevent adsorption and collapse of liquid droplets.

4. The droplet-based microfluidic device of Claim 1 further comprising a reaction chamber area that is configured to allow a chemical reaction to occur within said reaction chamber area, wherein said reaction chamber is connected to at least one set of the said plurality of micro-electrodes.

5. The droplet-based microfluidic device of Claim 4 further comprising a heating element that is operatively connected to the said reaction chamber area, wherein said heating element is configured to provide the necessary temperature zone within said reaction chamber area upon actuation.

6. The droplet-based microfluidic device of Claim 4, wherein said device comprises a plurality of reaction chamber areas that are configured to allow a simultaneous chemical reactions to occur within each of said reaction chamber area.

7. The droplet-based microfluidic device of Claim 6 further comprising a plurality of heating elements, wherein each of said heating element is operatively connected to each of said reaction chamber area, wherein each of said heating element is independently configured to provide the necessary temperature zone within each of said reaction chamber area upon actuation.

8. The droplet-based microfluidic device of Claim 5 further comprising a temperature detector element configured to detect the temperature zone within said reaction chamber area.

9. The droplet-based microfluidic device of Claim 6 further comprising a plurality of temperature detector elements, wherein each of said temperature detector element is individually configured to detect the temperature zone within each of said reaction chamber area.

10. The droplet-based microfluidic device of Claim 4 further comprising at least one reagent reservoir area operatively connected to said reaction chamber area.

11. The droplet-based microfluidic device of Claim 1, wherein said device is configured for conducting a polymerase chain reaction.

12. The droplet-based microfluidic device of Claim 11, wherein said device is configured for real-time polymerase chain reaction.

13. The droplet-based microfluidic device of Claim 11, wherein said device is configured for quantitative polymerase chain reaction.

14. The droplet-based microfluidic device of Claim 1, wherein said device is configured for amplifying nucleic acids.

15. The droplet-based microfluidic device of Claim 1, wherein said device is configured for conducting clinical diagnostic assay.

16. The droplet-based microfluidic device of Claim 1, wherein said device is configured for conducting real-time, quantitative polymerase chain reaction.

17. The droplet-based microfluidic device of Claim 1, wherein said device is configured for conducting a plurality of real-time, quantitative polymerase chain reactions in parallel.

18. The droplet-based microfluidic device of Claim 1, wherein said superhydrophobic material comprises a nano-textured dielectric layer and a fluoropolymer layer.

19. The droplet-based microfluidic device of Claim 18, wherein said fluoropolymer layer comprises fluorocarbon, fluorosilane, CYTOP®, or a mixture thereof.

20. The droplet-based microfluidic device of Claim 1, wherein the contact angle of a water droplet on said superhydrophobic material is at least 150°.

Application number / Numéro de demande: 2846963

Figures:

Pages: Sheet 1-8/16, Sheet 10-12/16,
Sheet 14/16, Sheet 16/16.

Unscannable items received with this application
(Request original documents in File Prep. Section on the 10th floor)

Documents reçu avec cette demande ne pouvant être balayés
(Commander les documents originaux dans la section de la préparation
des dossiers au 10ième étage)

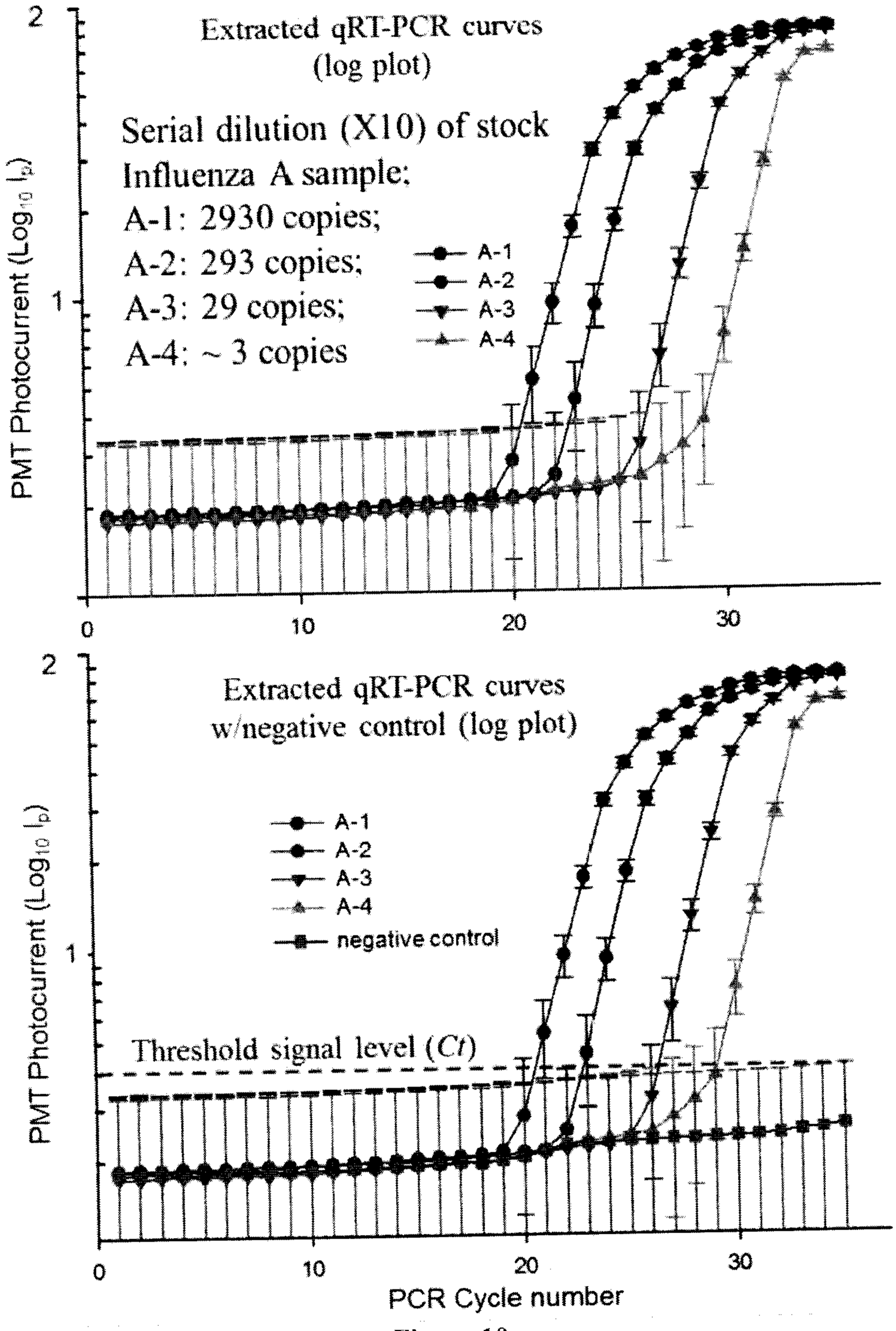
Extracted qRT-PCR curves
(log plot)
Serial dilution (X10) of stock
Influenza A sample;
A-1: 2930 copies;
A-2: 293 copies;
A-3: 29 copies;
A-4: ~ 3 copies
A-1
A-2
A-3
A-4
PMT Photocurrent (Log10 Ip)
2
1
0
10
20
30
Extracted qRT-PCR curves
w/negative control (log plot)
A-1
A-2
A-3
A-4
negative control
Threshold signal level (Ct)
PCR Cycle number

Figure 10

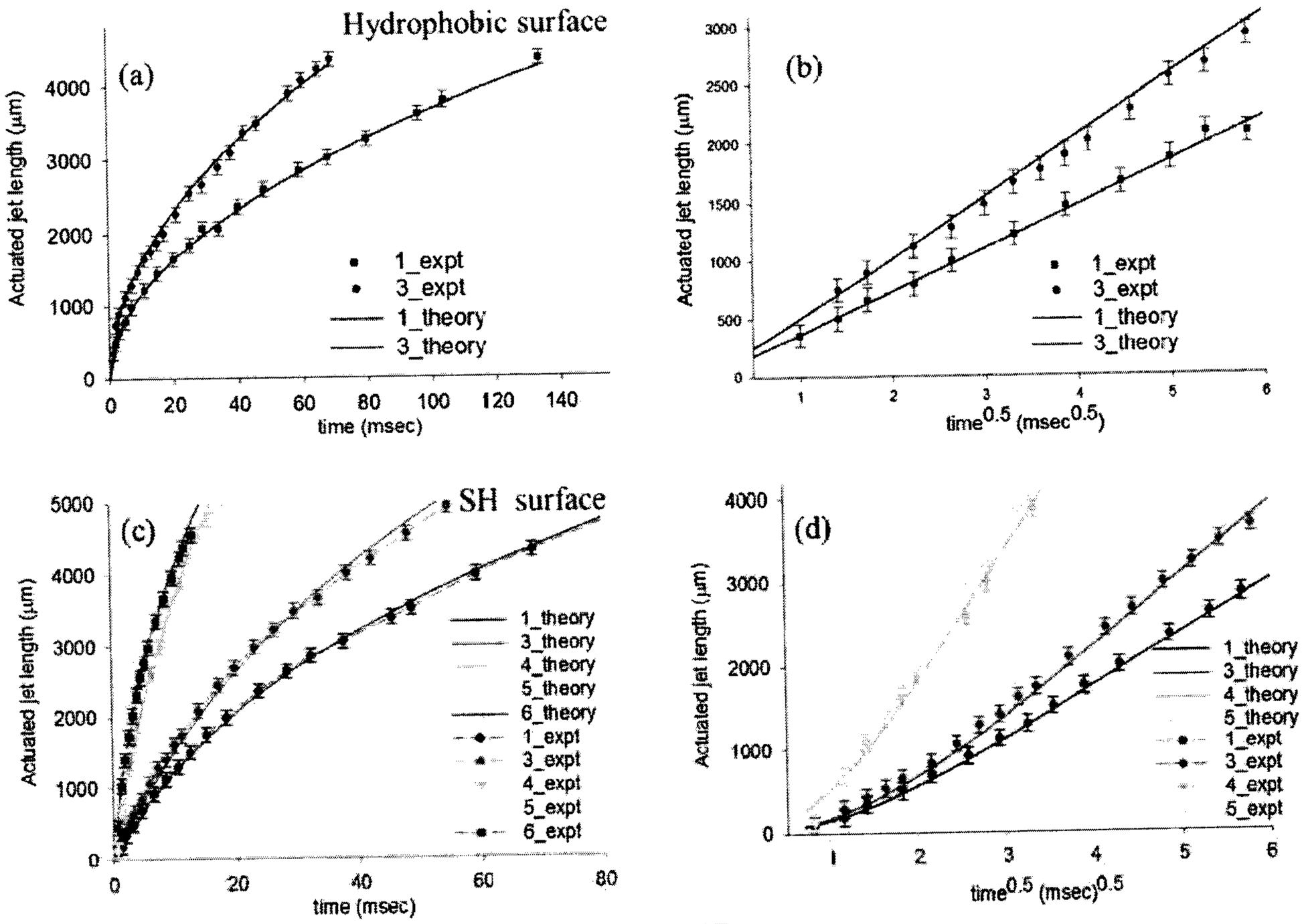

Figure 17

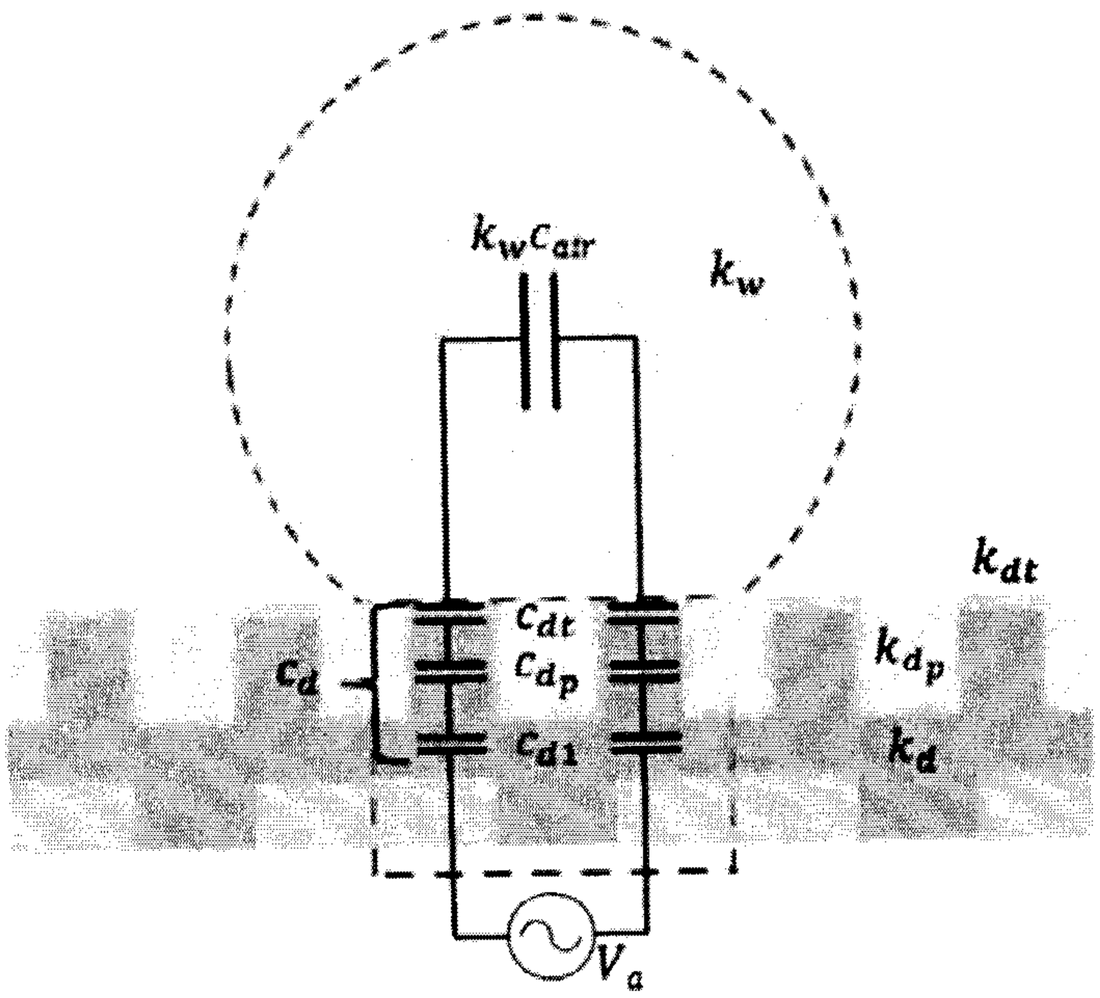

$$k_{dp} = \phi_s k_d + (1-\phi_s) k_{air};$$

$$c_{d1} = (\varepsilon_o k_d w)/d;$$

$$c_{dt} = (\varepsilon_o k_{dt} w)/dt;$$

$$c_{dp} = (\varepsilon_o k_{dp} w)/hp;$$

$$c_d = (1/c_{d1} + 1/c_{dt} + 1/c_{dp})^{-1};$$

$$c_{air} = (\varepsilon_o K(1-k^2))/(2K(k^2));$$

$$c_w = k_w c_{air}$$

$$\varepsilon_o = 8.854 \times 10^{-12}\, F/m$$

Figure 18

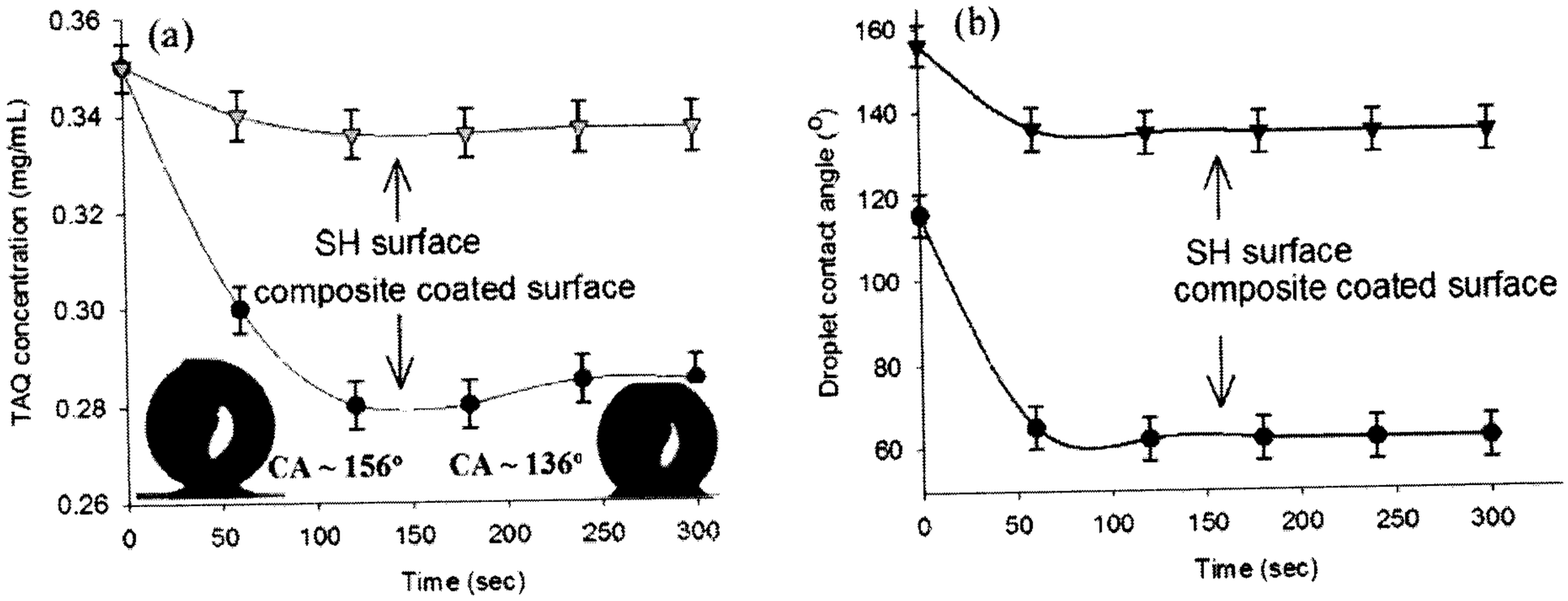

Figure 20

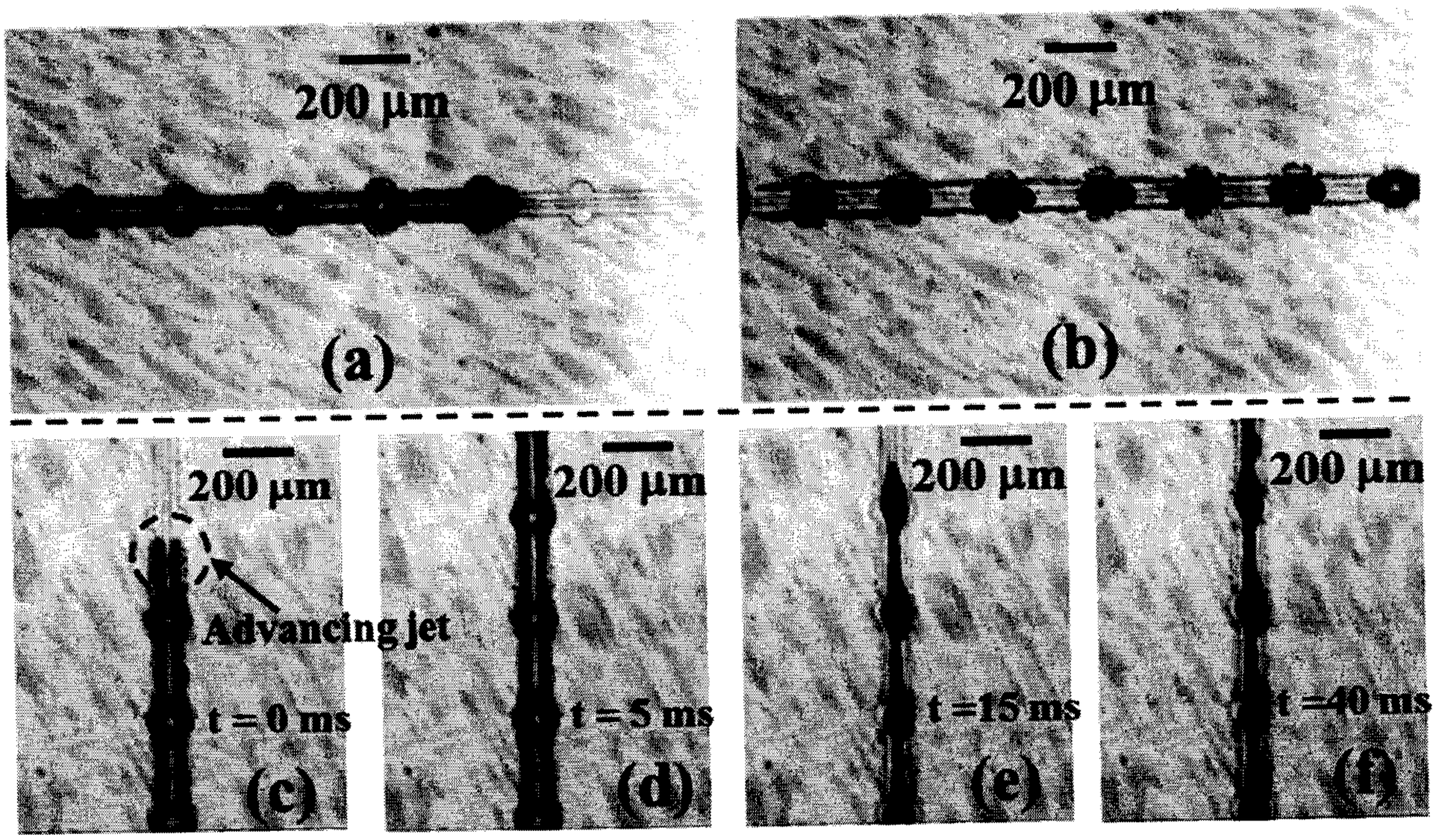

Figure 21